Laser direct write of heteroatom-doped graphene on molecularly controlled polyimides for electrochemical biosensors with nanomolar sensitivity

Ki-Ho Nam[a], **Moataz Abdulhafez**[a], **Elisa Castagnola**[b], **Golnaz Najaf Tomaraei**[a], **Xinyan Tracy Cui**[b], **Mostafa Bedewy**[a,c,d,*]

[a]Department of Industrial Engineering, University of Pittsburgh, 3700 O'Hara Street, Pittsburgh, PA, 15261, USA

[b]Department of Bioengineering, University of Pittsburgh, 3700 O'Hara Street, Pittsburgh, PA, 15261, USA

[c]Department of Chemical and Petroleum Engineering, University of Pittsburgh, 3700 O'Hara Street, Pittsburgh, PA, 15261, USA

[d]Department of Mechanical Engineering and Materials Science, University of Pittsburgh, 3700 O'Hara Street, Pittsburgh, PA, 15261, USA

Abstract

Fabrication of heteroatom-doped graphene electrodes remains a challenging endeavor, especially on flexible substrates. Precise chemical and morphological control is even more challenging for patterned microelectrodes. We herein demonstrate a scalable process for directly generating micropatterns of heteroatom-doped porous graphene on polyimide with different backbones using a continuous-wave infrared laser. Conventional two-step polycondensation of 4,4′-oxydianiline with three different tetracarboxylic dianhydrides enabled the fabrication of fully aromatic polyimides with various internal linkages such as phenylene, trifluoromethyl or sulfone groups. Accordingly, we leverage this laser-induced polymer-to-doped-graphene conversion for fabricating electrically conductive microelectrodes with efficient utilization of heteroatoms (N-doped, F-doped, and S-doped). Tuning laser fluence enabled achieving electrical resistivity lower than ~13 Ω sq^{-1} for F-doped and N-doped graphene. Finally, our microelectrodes exhibit superior performance for electrochemical sensing of dopamine, one of the important neurotransmitters in the brain. Compared with carbon fiber microelectrodes, the gold standard in electrochemical

dopamine sensing, our F-doped high surface area graphene microelectrodes demonstrated 3 order of magnitude higher sensitivity per unit area, detecting dopamine concentrations as low as 10 nM with excellent reproducibility. Hence, our approach is promising for facile fabrication of microelectrodes with superior capabilities for various electrochemical and sensing applications including early diagnosis of neurological disorders.

Keywords

Laser-induced graphene; Heteroatom self-doping; Porous nanocarbon; Electrochemical biosensors; Flexible devices; Microelectrodes

1. Introduction

Carbonaceous printed electrodes (CPE) are ubiquitous in many emerging technologies, including flexible electronics, energy storage/conversion devices, adsorption/separation membranes, electrocatalytically active materials, high sensitivity biosensors, and substrates for cell biology studies [1–4]. Although, sp^2-hybridized graphitic structures with diverse morphologies have been shown to exhibit unique physicochemical properties such as thermal stability, chemical inertness, and biocompatibility [5], their electrochemical performances are hindered by the absence of a bandgap [6]. The bandgap of CPE largely depends on additional holes, defect-rich heteroatom-doped sites, and pore structure and distribution [7,8]. Doping of heteroatoms either electron-withdrawing (p-type dopant) or electron-donating species (n-type dopant) into carbon domains results in both opening a bandgap and redistribution of charge, which tunes the electrochemical active sites and greatly broadens the scope of applications [9–11]. In addition, introduction of pores and structural defects also opens a bandgap, further enabling tunability of electrochemical behavior [12,13].

It is important to note here that doping graphene with a variety of different types of heteroatoms is routinely shown in literature to increase its electrocatalytic effect, whether the dopant atom/group was electron-withdrawing or electron-donating, and whether the dopant is a single type of heteroatom or a combination of dopants [14]. Accordingly, not any approach for doping graphene is equally impactful, because merely showing an improvement in electrochemical measurements resulting from doping in and of itself does not constitute an impactful finding in the absence of a clear advantage from a fabrication perspective. Importantly, in the typically solution-processed CPEs, it is still challenging to control the irreversible aggregation-driven reduction of available surface area, as well as the uncontrollable heteroatom-doping at the molecular level [15,16]. Hence, more effective fabrication methods are sought after for scalable manufacturing of CPEs with tailored chemistry and morphology, especially on flexible substrates.

An alternative strategy to effectively introduce heteroatoms, while controlling the 3D porous structure of nanocarbons is the so-called "bottom-up approach", wherein the chemistry and morphology of graphitic nanocarbons are simultaneously controlled during bottom-up synthesis directly on a dry substrate [17,18]. Laser-induced graphene (LIG) grown directly from polyimide (PI) and its commercially available derivative Kapton®, upon

laser irradiation has attracted considerable attention in recent years due to its capability as a process to create large surface area graphenic materials with tunable pore volume for superior electrode configuration [17,19]. From a fabrication perspective, this approach uniquely enables direct-writing of functional graphene electrodes on flexible substrates with facile patterning and high throughput production. Moreover, the capability to create a variety of morphologies, ranging from porous 3D graphene to aligned nanofibers [20–23], makes this laser-induced nanocarbon (LINC) fabrication technique promising for various applications including sensors [24,25], actuators [26,27], energy harvesters [28], smart filters and coatings [29,30], to functional composites [31]. Although, the porous morphology, atomic structure and chemical composition of LIG are controllable by tuning the laser parameters such as laser power, raster speed, laser spot size, and spot overlap [21,23,32,33], they are still in general chemically limited to C with small O and N content originated from imide ring in Kapton® [21,34].

Hence, heteroatom-doping strategies for LIG are needed to further tailor their properties for electrochemical sensing applications. A controlled gas atmosphere with O_2, Ar, H_2 or SF_6 during laser induction process influences the atomic percentages of C, O, and F in LIG [30]. The *ex situ* doping approaches have introduced small molecules (*e.g.*, H_3BO_3) into the PI matrix [35] or deposited polyaniline or metal oxides (*e.g.*, FeOOH and MnO_2) [28] on LIG followed by re-lasing. Despite its advantageous doping effect, the current approaches require the use of a controlled chamber environments, additive chemicals, or multi-step processes, thus complicating the LIG fabrication technique, and limits the simple, rapid, and scalable fabrication of LIG-based devices. For implementing practical microsystems, a facile way to achieve controllable chemical composition and hierarchical porous structure of LIG is still sought after.

The present study was motivated by the need to develop cost-competitive highly sensitive graphene-based microelectrodes for flexible/wearable electrochemical biosensors. Previous efforts towards this end have reported on different fabrication approaches, including screen-printed graphene [36], graphene aerogels [37], post-deposition annealed graphene ink [38], and graphene combined with metal particles [39] to increase the selectivity of neurotransmitter detection down to nanomolar (nM) level. Despite the remarkable increase in sensing sensitivity in some of these previous studies, the fabrication of graphene-based biosensors is still limited by requiring the following: (1) the addition of metal nanoparticle additives that complicates the fabrication process, (2) incorporating high-temperature annealing steps that are not compatible with flexible substrates; (3) complex multi-step lithography that greatly limits the scalability and practicality of fabrication, (4) pattern transfer approaches (from rigid substrates to flexible substrates) that both compromise properties and hamper productivity; and/or (5) employing conventional fabrication technologies that limit the resolution to millimeter-scale (of several-hundred-micron-scale) channels [38,40]. On the other hand, our work here on fabricating LIG microelectrodes directly on flexible polymer substrates in a one-step manufacturing process expands the range of applications for biosensing that require flexibility and bioimplantability while avoiding the need for complex and time-consuming procedures [41,42]. Nevertheless, despite its demonstrated potential and broad applicability, LIG on PI suffers from a major limitation represented by the commercially-available chemical

formulations of PI, which has been largely limited to commercial Kapton®. Therefore, if LIG microelectrodes are to become an effective technological solution for biosensing and other electrochemical applications, fabrication of LIG on tailored PIs is needed. In particular, creating capable neural probes for neurotransmitter detection requires sensitivity in the nM range, highlighting the importance of designing the molecular structure of PI substrates that can result in tunable microelectrode properties.

Herein, we demonstrate a one-step direct laser writing to simultaneously modulate the nano-/microscale morphology and heteroatom self-doping of the hierarchical porous nanocarbon (regularly evolving physicochemical architecture from graphene to fiber-like structure) from various PI chemical backbones by using a 10.6 μm continuous-wave CO_2 infrared laser. Our methodology based on molecular control of PI can be used effectively to tailor heteroatom compositions of the resulting LIG without the need for external doping sources such as gas atmosphere and additive molecules. Accordingly, we show that N-doping is derived from the imide group, while tetracarboxylic dianhydrides with different internal linkages (*e.g.*, trifluoromethyl and sulfone groups) act as a significant doping source of F and S heteroatoms. We also find that the nano-/microscale morphology and electrochemical properties of the doped LIG are strongly correlated to the molecular building blocks present in PI backbone structure. Finally, we demonstrate that these new class of heteroatom self-doped LIG microelectrodes have nanomolar sensitivity for the detection of dopamine (DA), a neurotransmitter in the brain that plays critical roles in many brain functions including movement, reward and emotion. Hence, our doped LIG fabrication approach is a compelling superior alternative to existing carbon-based microelectrode technologies, as they are promising for scalable manufacturing of flexible neurotransmitter sensors directly from a single polymeric material without any surface coating or composites.

2. Experimental section

2.1. Materials

Pyromellitic dianhydride (PMDA), 4,4'-(hexafluoroiso propylidene)diphthalic anhydride (6FDA), 3,3′,4,4′-diphenylsulfonetetracarboxylic dianhydride (DSDA), and 4,4′-oxydianiline (ODA) were purchased from Tokyo Chemical Industry, Co., Ltd. (Japan). 1-Methyl-2-pyrrolidinone (NMP) was purchased from Sigma-Aldrich (USA). All chemicals were used without further purification.

2.2. Synthesis of polyimides

From the literature, we identify the baseline type of graphene obtained from lasing PI to be N-doped, which is the typical LIG derived from Kapton® [17]. Hence, in order to systematically investigate the effect of internal linkage groups of fluorinated and sulfonated tetracarboxylic dianhydrides of PIs on graphene formation, the precursor PMDA–ODA, broadly known as Kapton®, was prepared as control to be compared to the precursor 6FDA–ODA containing trifluoromethyl groups and the precursor DSDA–ODA containing sulfone groups. Using a thermal imidization protocol, different PIs were synthesized from diamine ODA and three different tetracarboxylic dianhydrides, PMDA, 6FDA, and DSDA, *via* conventional two-step procedures, which include ring-opening polyaddition and subsequent

cyclic dehydration. The polymerization was carried out by reaction equimolar amounts of diamine with tetracarboxylic dianhydride at a concentration of 11–16 wt% solid in anhydrous NMP. Polycondensation was performed at 23 °C for 24 h and yielded viscous poly(amic acid) (PAA) intermediate solution. The PAA solution was poured onto a clean glass substrate, which was then placed on a level table and coated using a high precision adjustable film coating applicator with a blade gap of 1000 μm. The PAA was thermally cured by sequential temperature programming (90 °C/2 h, 150 °C/1 h, 200 °C/1 h, 250 °C/30 min, and 300 °C/30 min). Finally, the PI film was stripped off the glass substrate with the aid of deionized water and further dried in a convection oven at 70 °C for 6 h.

2.3. Preparation of heteroatom-doped nanocarbon patterns

The PMDA–ODA, 6FDA–ODA, and DSDA–ODA films with an average thickness of 70 μm were used as three different nanocarbon precursors. Direct laser engraving/cutting system (Full Spectrum Laser Pro-Series 20×12 platform, 1.5 inch focus lens) equipped with a continuous-wave CO_2 laser with wavelength of $\lambda_0 = 10.6$ μm was employed to locally carbonize of PI films. The laser objective lens is mounted on a motorized X–Y control stage with a maximum speed of 500 mm s^{-1} in one direction (X-axis). The experiments were performed with multiple combinations of laser power (P) and raster speed (S) at constant distance of laser beam waist to the surface of PI film (D) by fixing the sample stage vertically (Z-direction) with respect the objective lens [20]. The Gaussian laser beam diameter of beam waist by Knife Edge method is estimated to be 251.6 μm as described in our previous work [20]. The laser scribing was carried out in the range from 12.5 to 28.1 W of laser power with X-direction raster speed of 49–491 mm s^{-1} (See Table S1 in the supplementary information for a list of processing conditions and the corresponding laser fluence). RentinaEngrave 3D software was employed to design a single-line lasing to fabricate our microelectrodes on PI films without the need for any overlapping between multiple laser traces. All the laser scribing experiments were performed under ambient conditions.

2.4. Characterization

Attenuated total reflection–Fourier transform-infrared (ATR-FTIR) spectra were obtained with a Bruker VERTEX-70LS. Optical microscopy (OM) was performed with a Celestron handheld digital microscope, and the images were analyzed by Micro Capture Pro software. The mean line width and standard deviation were calculated for over 5 samples. Scanning electron microscopy (SEM) was performed using a Zeiss SIGMA VP high resolution field emission instrument at an acceleration voltage of 2 kV. Raman spectra were recorded on a Renishaw Raman microscope using a 633 nm laser excitation at room temperature with a laser power of 5 mW. X-ray photoelectron spectroscopy (XPS) measurements were performed using a Kα-spectrometer equipped with an Al–Kα micro-focused monochromator. For the C1s core XPS spectra, binding energies are offsetted in order to compensate for a slight shift of the sp^2 component to lower binding energy (283.5 eV relative to typical carbon materials 284.5 eV) [43], as this negative shift is not caused by changes in the chemical state, but is instead attributed to electrostatic interactions [43–45]. XRD was conducted on a Bruker D8 Discover SRD X-ray diffractometer with Cu Kα radiation ($\lambda = 1.54$ Å). The electrical resistance was measured using a Keithley two-point

probe meter (model: 2100, detection limit: 100 MΩ). Thermogravimetric analysis (TGA) was conducted with a TA Instruments Q500 under N_2 flow at a heating rate of 20 °C min^{-1}.

2.5. Electrode resistivity measurements

The electrical conductivity was measured using a Keithley two-point probe meter (model: 2100, detection limit: 100 MΩ). The electrical resistance value (R) of a single line electrode largely depends on three parameters: resistivity, length, and width. According, in order to calculate the electrode resistivity of our single line electrodes, the measured resistance (R) was divided by line length (L) in order to obtain a measure of resistance that is not dependent on length. This R/L value was calculated from multiple resistance measurements at different distances along the line. To convert R/L to the reported electrode resistivity (R_s) that does not depend on either length or width of the line electrodes (results plotted in Fig. 4), the R/L value was then multiplied by the line width (W), where $R_s = R/L \times W$. For clarification, the following equation explains the relationship between the different measures of resistance/resistively: $R = \rho\frac{L}{A} = \rho\frac{L}{W \times t} = R_s\frac{L}{W}$, where ρ is the resistivity of the material in Ω.m, and Rs is the electrode resistivity in Ω.sq^{-1}, which is analogous to sheet resistance for thin films. Here, t is the thickness of the electrode, which we do not need to measure if we use R_s. All measurements were performed on a minimum of five different electrodes to provide standard deviations in the resistivity values, represented as error bars in Fig. 4.

2.6. Fast scan cyclic voltammetry (FSCV) electrochemical detection

FSCV were performed with an EI 400 potentiostat (Ensman Instruments; Bloomington, IN, USA), controlled by the CV Tar Heels LabVIEW program (CV Tar Heels v4.3, University of North Carolina, Chapel Hill, NC, USA). The headstage gain was set to 5 MΩ. Data were analyzed using HDCV software (UNC Chapel Hill). The electrode was scanned from −0.4 to 1.0 V (vs. Ag/AgCl) and back with a 400 V s^{-1} scan rate and a repetition rate of 10 Hz. DA detection was identified by inspection of background-subtracted cyclic voltam-mograms. *In vitro* DA (Dopamine hydrochloride, Sigma-Aldrich, St. Louis, USA) calibration were performed using freshly prepared, nitrogen-purged DA standard solutions dissolved in 1xphosphate buffered saline (PBS). Electrode sensitivities were determined by the linear regression slope of the maximum faradaic current vs. DA concentration calibration plots.

3. Results and discussion

First, we demonstrate the potency of our polymer-to-doped nanocarbon conversion. We carbonized the PI films with different internal linkages using a 10.6 μm CO_2 infrared laser under ambient conditions to systematically analyze the effect of chemical structure of PI on characteristics of resulting LIG patterns. The experimental strategy is schematically shown in Fig. 1(a)–(b), followed by a detailed description of the individual steps. A variety of PI films were synthesized from ODA and corresponding tetracarboxylic dianhydrides (*i.e.*, PMDA, 6FDA, and DSDA) *via* two-step polycondensation. The exothermic polymerization was carried out by reacting equimolar amounts of ODA with tetracarboxylic dianhydrides at a concentration of 11–16 wt% solid in NMP. The precursor PAAs are converted into the corresponding PIs through a thermal imidization, which corresponded to cyclization

dehydration (see Supplementary Fig. S1(a) and related discussion). With computer-programmed laser scribing, heteroatom-doped LIG can be readily written directly on PI films. Visibly black lines were generated on the free-standing flexible PI films after the laser scribing confirming the localized carbonization of the polymer (Fig. 1(c)). To collectively refer to all laser-induced nanocarbon materials including 3D graphene with different nanoscale and mesoscale morphologies, we use the acronym LINC in this work [20]. Also, we denote the resulting nanocarbon material by the dominant heteroatom content as follows: N-LINC for lased lines on PMDA–ODA, F-LINC for lased lines on 6FDA–ODA, and S-LINC for lased lines on DSDA–ODA, respectively.

Precise tuning of nanocarbon structure and line dimension on different backbones of the three PI films was achieved by adjusting the laser processing parameters. Fig. 2(a)–(c) shows a map correlating the resulting LINC morphology to both laser power (P) and raster speed (S). We successfully demonstrate the formation of a diverse set of nanocarbons ranging from continuous porous graphene to wooly fibrous morphologies. It indicates that with the increase of laser power at a constant defocus (distance of laser beam waist to the surface of film), the raster speed also needs to be increased to achieve stable carbon line and prevent excessive ablation of PI. It could also be clearly seen that the graphitization efficiency and nano-/microscale morphology depended strongly on the chemical structure of the PIs. The morphological transition from the electrically conducting porous morphologies to the high resistivity wooly nanofibers, occurred at a lower laser fluence (i.e. lower power and higher speed) for S-LINC, compared to F-LINC. In general, N-LINC is most stable at higher laser fluence values (discussed below). We have previously shown that this transition is important for fabrication of functional graphene electrodes with good electrical conductivity [20].

Fig. 2(d)–(f) shows that SEM surface morphologies of the laser-written lines exhibit a foam-like arrays with micropores (laser power of 12.5 W, raster speed of 500 mm s^{-1}). Cross-sectional images, as shown in Fig. S2(a)–(c), reveal an ordered hierarchical porous structure consisting of a cellular network covering the top of the porous foam. The volume of the cellular networks obtained at the same laser conditions were bigger for S-LINC followed by F-LINC, and then N-LINC. At lower speeds (higher fluence) we observe ablation for the low-density cellular networks at the center of the lased lines (see the cross-sectional SEM images in Supplementary Fig. S2(d)–(f)). The porous structure obtained at the slowest raster speed of 47 mm s^{-1} (at laser power of 12.5 W) exhibits a bimodal distribution with a few relatively large pores dispersed separately in an interconnected porous skeleton formed by small pores without any cellular network (Fig. 2(g)–(i)). The average pore size has been enlarged to a value of 1.87 μm for S-LINC compared to corresponding average pore size of the N-LINC (1.69 μm), as estimated from electron microscopy. The increase in pore size as well as cellular network of F- and S-doped LINC relative to the N-LINC is ascribed to rapid liberation and release of more gaseous decomposition products during transient local photothermal reaction [28,46,47]. These distinct differences in nanocarbon growth and their nano-/microscale morphology strongly reflect the molecular chain packing and inherent thermal properties of the three different types of PI (see Supplementary Fig. S1(b)–(c) and related discussion).

To qualitatively investigate the effect of molecular building blocks of PIs on carbon line features under varying laser parameters, the carbonized lines were firstly prepared using raster speed ranging from 47 to 500 mm s^{-1} in increments about 100 mm s^{-1} at a constant laser power of 12.5 W. The laser fluence, corresponding each laser processing parameter was increased gradually from 16 to 170 J cm^{-2} on the PI films. The detailed description of the laser fluence calculation from the Gaussian beam modeling is provided in a Supplementary Note.

Raman spectroscopy was used to characterize structural transformations in LINC lines that were formed on the three PI films. Deconvolution of the spectra from all N-LINC, F-LINC, and S-LINC lines was carried out based on five characteristic bands (see Supplementary Fig. S3): the I-, D-, and D′-band at ~1120 cm^{-1}, ~1350 cm^{-1}, and ~1610 cm^{-1} corresponding to the sp^3 hybridization and disordered carbon domains including vacancies and edges [48]; the D″-band at ~1500 cm^{-1} corresponding to contributions from the phonon density of states due to small size graphitic crystals or hydrogenated carbons [49,50]; and the G-band at ~1580 cm^{-1} originating from sp^2 bonds from perfectly organized hexagonal carbon domains with contributions from possible double bonds [51,52]. Moreover, the second order 2D-band at 2650 cm^{-1} is considered, which is characteristic of graphenic nanocarbons [51–54]. In Fig. 3(a), the 2D-band is hardly distinguishable in N-LINC obtained at laser fluence of 16 J cm^{-2}, while in the F- and S-doped LINC cases an intense resonance is revealed with a symmetrical profile centered at 2650 cm^{-1}. In addition, significant improvements in the 2D/G ratio were observed in F-LINC and S-LINC, compared to N-LINC, under laser fluence of 16 J cm^{-2}, indicating higher photothermal conversion capabilities of 6FDA–ODA and DSDA–ODA at low laser energy compared to PMDA-ODA (Fig. 3(b)).

Interestingly, carbonization of S-LINC at laser fluence of 170 J cm^{-2} (Fig. 3(c)) resulted in a distinctly higher D/G (Fig. 3(d)), and concomitantly stronger and sharper D-band characteristics (Fig. 3(c)) compared to N-LINC and F-LINC. This is attributable to the partial photothermal oxidation of graphitic structure in S-LINC originating from oxygen-rich polymer backbone of DSDA–ODA during laser scribing in air. Comparing the D/D′ ratios for all three types of doped graphene (Fig. S4) reveals relatively similar values in the range of 3.5–4.5, which indicates that the types of defects causing disorder are similar in N-LINC, F-LINC, and S-LINC, and are likely dominated by edge defects and vacancies, as opposed to sp^3 defects [48]. Further, comparing the D″ peak size fitted for all three types (N-LINC, F-LINC, and S-LINC) at low fluence (16 J cm^{-2}) and high fluence (170 J cm^{-2}) reveals that D″-band is greatly diminished at higher fluences, which suggests improved graphenic crystallinity with laser fluence (see Supplementary Fig. S5) [55,56].

For all three types of LINC in our study (N-LINC, F-LINC, and S-LINC), the XRD patterns (see Supplementary Fig. S6) show strong (002) and (100) peaks centered at 2θ = 26.3 and 2θ = 43.5, respectively, giving an interlayer spacing (*d*-spacing) of ~3.4 Å between adjacent (002) lattice planes, and indicates a high degree of graphitization [57], which corroborates the Raman spectroscopy results presented above.

To extend the compositional analysis of laser-treated PIs, XPS characterization of chemical binding was conducted (see Supplementary Fig. S7). In all cases, the graphitization of

the PIs becomes clear by the appearance of the dominant sp^2 carbon in C1s peak with considerably smaller O1s and N1s peaks (see Supplementary Figs. S7–S10). In Fig. 3(e)–(g) (plotted from data in Supplementary Table S2), with increase in laser fluence, the calculated atomic percentages of carbon sharply increase from original 68–75% in three PI films to 89–95% in LINC lines. The remarkable decline of oxygen and nitrogen content at high laser fluence indicates that the correspondingly high temperatures induced by the laser triggered the effective graphitization of the PI. The fluorine and sulfur signals in F-LINC and S-LINC also show a slight decrease, however are clearly present even at the highest laser fluence of 170 J cm^{-2}.

Fig. S8(a)–(b) show the high resolution C1s XPS spectra of the PMDA-ODA before and after the laser carbonization (at 52 J cm^{-2}), respectively. The deconvoluted C1s spectrum for N-LINC is represented by four different deconvolved peaks (see Table S3 in the supplementary material): sp^2 hybridized carbon at 284.5 eV, sp^3 hybridized carbon/C–N bonds at 286.3 eV, epoxide/hydroxyl C–O bonds at 287.8 eV, and carbonyl O=C–O bonds at 289.8 eV, which agree with previously published results [17,58]. For both F-LINC (Fig. S9(a)) and S-LINC (Fig. S10(a)), the peak representing sp^3 carbon/C–N bonds is observed at almost the same binding energy (at 286.0 eV and 285.9 eV respectively), indicating that C–N bonds exist in all three cases, although N is the dominant dopant in the case of N-LINC. On the hand, in the case of F-LINC the presence of a peak at 292.7 eV representing C–F bonds confirms the effective F-doping. Similarly, in the case of S-LINC the presence of a peak at 287.2 eV representing C–S bonds confirms the effective S-doping.

In addition, the high resolution F1s spectrum of the F-LINC clearly reveals C–F bonds with neighboring C atoms at 686.8 and 687.7 eV, which were associated with semi-ionic C–F and covalent C–F bonds (see Supplementary Fig. S9(b)) [59]. In Fig. S10(b), the high resolution S2p spectrum of the S-LINC exhibit peaks for oxidized sulfur groups [60,61], which agrees with the Raman analysis. The spatially localized transient laser irradiation could result in extremely high temperatures, and the generated high energy leads to lattice vibrations [47]. During laser scribing, the atoms in lattice structure would be reintegrated or released as gases, and the rest of the heteroatoms and aromatic compounds would be rearranged to generate doped graphenic patterns.

The effective heteroatom-doping into the largely sp^2 carbon provides excess electrons in the carbon framework, enabling high electrical conductivity [60]. While the laser parameters enables us to control both the morphology and chemical doping of LINC, further change in the macroscopic electrode line dimensions for electrochemical sensing provides an additional way to tune the electrode resistivity (R_s). In general, resistivity gradually increased as the raster speed increases to 500 mm s^{-1} (as opposed to laser fluence, see Supplementary Fig. S11) at constant laser power of 12.5 W, but changes in heteroatom-doping ratio and line width cause noticeable differences in resistivity of three types of patterns (Fig. 4(a)–(b)). Given a constant high-speed lasing in Fig. 4(c)–(d), electrical sensing area of N-LINC and F-LINC was found to be proportional to the patterns of different widths caused by laser power. Above the laser power of 18.3 W, however, the resistivity of S-LINC is drastically increased to >1.685 KΩ sq^{-1}. This can be explained by the difference in photothermal interactions from the radiation absorption by the PI

substrates, which drive a temperature increase that thermally oxidizes S-LINC and forms large volume woolly fibrous structure under the same laser conditions (Fig. 4(e)–(f)) [20]. Importantly, F-LINC exhibits low resistivity in all laser processing window with a minimum value of ~13 Ω sq^{-1}.

To study the electrochemical sensitivity of the three different high surface area heteroatom-doped LINC microelectrodes, we evaluate the *in vitro* catecholamine neurotransmitters detection capability in a range of concentration from 10 nM to 1 μM in PBS, using fast scan cyclic voltammetry (FSCV). DA is an electroactive compound capable of reversible oxidation to dopamine-*o*-quinone (DAoQ) upon application of a sufficient potential, following a two-electrons and two-protons exchange (Fig. 5(a) left) [62–64]. Using FSCV, DA is typically detected through a triangular waveform with a scan rate of 400 V s^{-1} applied repeatedly at 10 Hz, starting from an holding potential of –0.4 V (vs. Ag/AgCl), applied to the working electrode, to selectively preconcentrate cationic DA on the electrode surface [64–66], to a switching potential of +1.0/+1.3V and back to the holding potential to oxidize DA and reduce DAoQ (Fig. 5(a) right).

Fig. 5(b) presents FSCV background current in 1x PBS (lines) and after the injection of 500 nM DA (scatters) for N-LINC (black), F-LINC (red), and S-LINC (blue), respectively. After the background subtraction, the CV plots exhibit characteristic anodic DA oxidation and cathodic DAoQ reduction peaks, confirming the detection of DA (Fig. 5(c)). Fig. 5(d)–(f) reports the background subtracted CV plots corresponding to the detection of 10, 100, 250, 500 nM and 1 μM bolus of DA injection, for N-LINC, S-LINC, and F-LINC, respectively. The DA oxidation peaks linearly increase with the concentrations, as confirmed by the linear regression fit of the calibration curve, that plots the maximum faradaic oxidation current *versus* DA concentration, in Fig. 5(g).

The sensitivity towards DA, based on the linear regression slope of the calibration curve, is determined to be 4.23 ± 0.03 nA nM^{-1} (Mean ± SD, n = 7), 4.25 ± 0.11 (Mean ± SD, n = 7), and 5.78 ± 0.32 nA nM^{-1} (Mean ± SD, n = 7) for N-LINC, S-LINC, and F-LINC, respectively. The sensitivity normalized by the geometric area, as reported in Fig. 5(g), is highest for F-LINC (47% higher than N-LINC), followed by S-LINC (22% higher than N-LINC), with N-LINC being the lowest. All LINCs have area-normalized sensitivities three order of magnitude greater than what has been reported in literature from carbon fiber microelectrodes (CFEs) (4.9 ± 0.5 nA μM^{-1} and 13 ± 2 nA μM^{-1}) [63,67].

The current peak in response to 1 μM DA by the geometric area is 70.78 ± 3.75 pA μm^{-2}, 101.69 ± 7.61 pA μm^{-2}, and 112.89 ± 3.11 pA μm^{-2} for N-LINC, S-LINC, and F-LINC, respectively. These values are comparable to the value observed for high-sensitivity and high surface area microelectrodes reported in literature, such as carbon nanotube (CNT) (82 ± 10 pA μm^{-2}) [68], CNT/coated carbon fiber microelectrodes (CFE) (100 ± 25 pA μm^{-2}) [68], and CNT/polyethylenimine (PEI) fibers (122 ± 23 pA μm^{-2}) [69]. Remarkably, the three different doped LINC microelectrodes can detect 10 nM DA concentration with clear discrimination of the oxidation and reduction peaks (Fig. 5(d)–(f), insets). The results indicate that the doped LINC microelectrodes can be used for highly sensitive DA detection with FSCV.

Other than higher sensitivity, F-LINC also exhibits a lower peak-to-peak potential separation (ΔE_p) value (ΔE_p 0.75 = ± 0.01V) compared to S-LINC (ΔE_p = 0.80 ± 0.02 V) and N-LINC (ΔE_p = 0.80 ± 0.03 V), indicative of faster electron transfer kinetics. The effects of dopant types/functionalization on LINC DA sensitivity may be described with following mechanisms: (i) aromatic π–π stacking interactions between the ammonium cation of the protonated DA and π electrons of the hexagonal ring in the carbon surface; (ii) electrostatic or chemical bonding interactions between the NH_3^+ cations of the protonated DA at neutral pH and negative charges on the carbon, as previously observed for graphene oxide and CNTs [70,71]; (iii) strong hydrogen bonding between the most electronegative F element and DA [72]; (iv) increasing the number of catalytic active sites of the neighboring dopant *via* structural engineering (doping, defect sites, porous structures) and enhancing the DA adsorption [73]; (v) the lowest line width-normalized resistivity of F-LINC (Fig. 4(a)) and facilitation of electron transfer between DA and the F-doped electrode surface. The contribution of the different doping, with particular focus on the F-doping, for the purpose to enhance the sensitivity and the electrocatalytic activity of the doped LINC will be further investigated in a future study.

Hence, our combined results in this study on the process–structure–property relationship for the direct laser-induced formation of heteroatom-doped LIG demonstrates the following: (1) unprecedented control of LIG chemistry by *in situ* heteroatom self-doping during lasing based on molecularly engineered PI substrates; (2) combining chemistry control with fluence-dependent morphological transitions in LIG to pattern functional microelectrodes in a facile one-step manufacturing process that has a transformative potential in flexible device manufacturing; (3) fabricating electrochemical biosensors for detection of the neurotransmitter dopamine with nanomolar resolution.

4. Conclusion

In this study, we demonstrate a capable approach to fabricate doped graphene microelectrodes with controllable chemistry and porous morphology by laser-induced carbonization of molecularly engineered polyimides. In particular, we show that the chemical backbone structure of the precursor polymer can be used to tailor the chemical composition, nano-/microscale morphology, and performance of our fabricated electrochemical biosensors. Three different types of graphene electrodes were fabricated depending on the dominant heteroatoms (N-doped, F-doped, and S-doped), which are derived from the molecular building blocks of PIs. Importantly, our microelectrodes are directly doped during laser scribing, which is a significant advantage for manufacturing electrically conductive and electrochemically functional porous graphene. By modulating laser parameters, we find that the electrical resistivity of our F-doped graphene can be precisely tuned to lower than 161 Ω sq^{-1} at even quite low values of laser fluence (16 J cm^{-2}), compared to 572 Ω sq^{-1} for N-doped graphene. At higher fluence values, even lower resistivity is possible with a minimum of 13 Ω sq^{-1} measured in this study. Moreover, we tested the sensitivity of electrochemical sensors fabricated by our approach. While all three types of microelectrodes were capable of detecting target catecholamine neurotransmitters like dopamine with concentrations as low as 10 nM, our F-doped graphene electrodes

exhibited the highest sensitivity with excellent reproducibility, compared to the S-doped, and the N-doped. These findings on the process–structure–property relationships for direct laser-induced formation of heteroatom-doped graphene can be leveraged for the fabrication of other flexible devices, such as supercapacitors, electrocatalysts, and other functionalities in smart wearables.

Supplementary Material

Refer to Web version on PubMed Central for supplementary material.

Acknowledgements

References

[1]. Kamyshny A, Magdassi S, Conductive nanomaterials for printed electronics, Small 10 (2014) 3515–3535, 10.1002/smll.201303000. [PubMed: 25340186]

[2]. Zhang W, Zhu S, Luque R, Han S, Hu L, Xu G, Recent development of carbon electrode materials and their bioanalytical and environmental applications, Chem. Soc. Rev 45 (2016) 715–752, 10.1039/c5cs00297d. [PubMed: 26662473]

[3]. El-Kady MF, Kaner RB, Direct laser writing of graphene electronics, ACS Nano 8 (2014) 8725–8729, 10.1021/nn504946k. [PubMed: 25215512]

[4]. Fu K, Yao Y, Dai J, Hu L, Progress in 3D printing of carbon materials for energy-related applications, Adv. Mater 29 (2017) 1–20, 10.1002/adma.201603486.

[5]. Wang C, Xia K, Wang H, Liang X, Yin Z, Zhang Y, Advanced carbon for flexible and wearable electronics, Adv. Mater 31 (2019) 1–37, 10.1002/adma.201801072.

[6]. Oostinga JB, Heersche HB, Liu X, Morpurgo AF, Vandersypen LMK, Gate-induced insulating state in bilayer graphene devices, Nat. Mater 7 (2008) 151–157, 10.1038/nmat2082. [PubMed: 18059274]

[7]. Zhang S, Tsuzuki S, Ueno K, Dokko K, Watanabe M, Upper limit of nitrogen content in carbon materials, Angew. Chem. Int. Ed 54 (2015) 1302–1306, 10.1002/anie.201410234.

[8]. Liu Y, Jin Z, Wang J, Cui R, Sun H, Peng F, Wei L, Wang Z, Liang X, Peng L, Li Y, Nitrogen-doped single-walled carbon nanotubes grown on substrates: evidence for framework doping and their enhanced properties, Adv. Funct. Mater 21 (2011) 986–992, 10.1002/adfm.201002086.

[9]. Tang C, Zhang Q, Nanocarbon for oxygen reduction electrocatalysis: dopants, edges, and defects, Adv. Mater 29 (2017), 10.1002/adma.201604103.

[10]. Basu A, Roy K, Sharma N, Nandi S, Vaidhyanathan R, Rane S, Rode C, Ogale S, CO2 laser direct written MOF-based metal-decorated and heteroatom-doped porous graphene for flexible all-solid-state micro-supercapacitor with extremely high cycling stability, ACS Appl. Mater. Interfaces 8 (2016) 31841–31848, 10.1021/acsami.6b10193. [PubMed: 27809473]

[11]. Thearle RA, Latiff NM, Sofer Z, Mazánek V, Pumera M, Boron and nitrogen doped graphene via microwave exfoliation for simultaneous electrochemical detection of ascorbic acid, dopamine and uric acid, Electroanalysis 29 (2017) 45–50, 10.1002/elan.201600516.

[12]. Wu B, Li M, Xiao S, Qu Y, Qiu X, Liu T, Tian F, Li H, Xiao S, A graphyne-like porous carbon-rich network synthesized: via alkyne metathesis, Nanoscale 9 (2017) 11939–11943, 10.1039/c7nr02247f. [PubMed: 28786456]

[13]. Wang X, Ma X, Zhang L, Jiang G, Yang M, Dielectric and optical properties of porous graphenes with uniform pore structures, J. Mol. Model 25 (2019) 1–9, 10.1007/s00894-019-4127-z.

[14]. Wang L, Sofer Z, Pumera M, Will any crap we put into graphene increase its electrocatalytic effect? ACS Nano 14 (2020) 21–25, 10.1021/acsnano.9b00184. [PubMed: 31934742]

[15]. Paul R, Du F, Dai L, Ding Y, Wang ZL, Wei F, Roy A, 3D heteroatom-doped carbon nanomaterials as multifunctional metal-free catalysts for integrated energy devices, Adv. Mater 31 (2019) 1805598, 10.1002/adma.201805598.

[16]. Rocha VG, García-Tuñón E, Botas C, Markoulidis F, Feilden E, D'Elia E, Ni N, Shaffer M, Saiz E, Multimaterial 3D printing of graphene-based electrodes for electrochemical energy storage using thermoresponsive inks, ACS Appl. Mater. Interfaces 9 (2017) 37136–37145, 10.1021/acsami.7b10285. [PubMed: 28920439]

[17]. Lin J, Peng Z, Liu Y, Ruiz-Zepeda F, Ye R, Samuel ELGG, Yacaman MJ, Yakobson BI, Tour JM, Laser-induced porous graphene films from commercial polymers, Nat. Commun 5 (2014) 5714, 10.1038/ncomms6714. [PubMed: 25493446]

[18]. Ye R, James DK, Tour JM, Laser-induced graphene: from discovery to translation, Adv. Mater 31 (2019) 1803621, 10.1002/adma.201803621.

[19]. Ye R, James DK, Tour JM, Laser-induced graphene, Acc. Chem. Res 51 (2018) 1609–1620, 10.1021/acs.accounts.8b00084. [PubMed: 29924584]

[20]. Abdulhafez M, Tomaraei GN, Bedewy M, Fluence-dependent morphological transitions in laser-induced graphene electrodes on polyimide substrates for flexible devices, ACS Appl. Nano Mater 4 (2021) 2973–2986, 10.1021/acsanm.1c00101.

[21]. Lamberti A, Perrucci F, Caprioli M, Serrapede M, Fontana M, Bianco S, Ferrero S, Tresso E, New insights on laser-induced graphene electrodes for flexible supercapacitors: tunable morphology and physical properties, Nanotechnology 28 (2017) 174002, 10.1088/1361-6528/aa6615. [PubMed: 28282299]

[22]. Duy LX, Peng Z, Li Y, Zhang J, Ji Y, Tour JM, Laser-induced graphene fibers, Carbon N. Y 126 (2018) 472–479, 10.1016/j.carbon.2017.10.036.

[23]. Wang R, Duan X, Yao J, Ruan X, Yao Y, Liu T, Processing–structure–property relationship in direct laser writing carbonization of polyimide, J. Appl. Polym. Sci 137 (2020) 1–13, 10.1002/app.48978.

[24]. Getachew BA, Bergsman DS, Grossman JC, Laser-induced graphene from polyimide and polyethersulfone precursors as a sensing electrode in anodic stripping voltammetry, ACS Appl. Mater. Interfaces 12 (2020) 48511–48517, 10.1021/acsami.0c11725. [PubMed: 33052656]

[25]. Tao LQ, Tian H, Liu Y, Ju ZY, Pang Y, Chen YQ, Wang DY, Tian XG, Yan JC, Deng NQ, Yang Y, Ren TL, An intelligent artificial throat with sound-sensing ability based on laser induced graphene, Nat. Commun 8 (2017) 1–8, 10.1038/ncomms14579. [PubMed: 28232747]

[26]. Zhang TY, Wang Q, Deng NQ, Zhao HM, Wang DY, Yang Z, Liu Y, Yang Y, Ren TL, A large-strain, fast-response, and easy-to-manufacture electro-thermal actuator based on laser-reduced graphene oxide, Appl. Phys. Lett 111 (2017) 121901, 10.1063/1.5003610.

[27]. Zhang C, Su JW, Deng H, Xie Y, Yan Z, Lin J, Reversible self-assembly of 3D architectures actuated by responsive polymers, ACS Appl. Mater. Interfaces 9 (2017) 41505–41511, 10.1021/acsami.7b14887. [PubMed: 29115816]

[28]. Li L, Zhang J, Peng Z, Li Y, Gao C, Ji Y, Ye R, Kim ND, Zhong Q, Yang Y, Fei H, Ruan G, Tour JM, High-performance pseudocapacitive micro-supercapacitors from laser-induced graphene, Adv. Mater 28 (2016) 838–845, 10.1002/adma.201503333. [PubMed: 26632264]

[29]. Yong J, Yang Q, Chen F, Zhang D, Farooq U, Du G, Hou X, A simple way to achieve superhydrophobicity, controllable water adhesion, anisotropic sliding, and anisotropic wetting based on femtosecond-laser-induced line-patterned surfaces, J. Mater. Chem. A 2 (2014) 5499–5507, 10.1039/c3ta14711h.

[30]. Li Y, Luong DX, Zhang J, Tarkunde YR, Kittrell C, Sargunaraj F, Ji Y, Arnusch CJ, Tour JM, Laser-induced graphene in controlled atmospheres: from superhydrophilic to superhydrophobic surfaces, Adv. Mater 29 (2017) 1–8, 10.1002/adma.201700496.

[31]. Nasser J, Zhang L, Sodano H, Laser induced graphene interlaminar reinforcement for tough carbon fiber/epoxy composites, Compos. Sci. Technol 201 (2021) 108493, 10.1016/j.compscitech.2020.108493.

[32]. Abdulhafez M, McComb AJ, Bedewy M, Tailoring surface hydrophobicity of commercial polyimide by laser-induced nanocarbon texturing, J. Micro Nano-Manufacturing 8 (2020) 1–9, 10.1115/1.4048600.

[33]. Nasser J, Lin J, Zhang L, Sodano HA, Laser induced graphene printing of spatially controlled super-hydrophobic/hydrophilic surfaces, Carbon N. Y 162 (2020) 570–578, 10.1016/j.carbon.2020.03.002.

[34]. Cai J, Lv C, Watanabe A, Cost-effective fabrication of high-performance flexible all-solid-state carbon micro-supercapacitors by blue-violet laser direct writing and further surface treatment, J. Mater. Chem. A 4 (2016) 1671–1679, 10.1039/c5ta09450j.

[35]. Peng Z, Ye R, Mann JA, Zakhidov D, Li Y, Smalley PR, Lin J, Tour JM, Flexible boron-doped laser-induced graphene microsupercapacitors, ACS Nano 9 (2015) 5868–5875, 10.1021/acsnano.5b00436. [PubMed: 25978090]

[36]. Walch NJ, Davis F, Langford N, Holmes JL, Collyer SD, Higson SPJ, Enhancement of electrode performance by a simple casting method using sonochemically exfoliated graphene, Anal. Chem 87 (2015) 9273–9279, 10.1021/acs.analchem.5b01829. [PubMed: 26289227]

[37]. Ai S, Chen Y, Liu Y, Zhang Q, Xiong L, Huang H, Li L, Yu X, Wei L, Facile synthesis of nitrogen-doped graphene aerogels for electrochemical detection of dopamine, Solid State Sci. 86 (2018) 6–11, 10.1016/j.solidstatesciences.2018.09.014.

[38]. Butler D, Moore D, Glavin NR, Robinson JA, Ebrahimi A, Facile post-deposition annealing of graphene ink enables ultrasensitive electrochemical detection of dopamine, ACS Appl. Mater. Interfaces 13 (2021) 11185–11194, 10.1021/acsami.0c21302. [PubMed: 33645208]

[39]. Palanisamy S, Ku S, Chen SM, Dopamine sensor based on a glassy carbon electrode modified with a reduced graphene oxide and palladium nano-particles composite, Microchim. Acta 180 (2013) 1037–1042, 10.1007/s00604-013-1028-1.

[40]. Abu-Ali H, Cansu O, Davis F, Walch N, Nabok A, Electrochemical aptasensor for detection of dopamine, Chemosensors 8 (2020), 10.3390/CHEMOSENSORS8020028.

[41]. Santos NF, Pereira SO, Moreira A, Girão AV, Carvalho AF, Fernandes AJSS, Costa FM, IR and UV laser-induced graphene: application as dopamine electrochemical sensors, Adv. Mater. Technol 2100007 (2021) 2100007, 10.1002/admt.202100007.

[42]. Soares RRA, Hjort RG, Pola CC, Parate K, Reis EL, Soares NFF, Mclamore ES, Claussen JC, Gomes CL, Laser-induced graphene electrochemical immunosensors for rapid and label-free monitoring of Salmonella enterica in chicken broth, ACS Sens. 5 (2020) 1900–1911, 10.1021/acssensors.9b02345. [PubMed: 32348124]

[43]. Sobol PE, Bomben KD, Moulder JF, Stickle WF, Handbook of X-ray photoelectron spectroscopy, Chastain, J, Perkin-Elmer Corp. Phys. Electron. (1992), 10.1002/0470014229.ch22.

[44]. Oswald S, Thoss F, Zier M, Hoffmann M, Jaumann T, Herklotz M, Nikolowski K, Scheiba F, Kohl M, Giebeler L, Mikhailova D, Ehrenberg H, Binding energy referencing for XPS in Alkali metal-based battery materials research (II): application to complex composite electrodes, Batteries 4 (2018) 1–19, 10.3390/batteries4030036.

[45]. Díaz J, Paolicelli G, Ferrer S, Comin F, Separation of the sp3 and sp2 and components in the C1s photoemission spectra of amorphous carbon films, Phys. Rev. B 54 (1996) 8064–8069, 10.1103/PhysRevB.54.8064.

[46]. El-Kady MF, Strong V, Dubin S, Kaner RB, Laser scribing of high-performance and flexible graphene-based electrochemical capacitors, Science 335 (2012) 1326–1330, 10.1126/science.1216744. [PubMed: 22422977]

[47]. Dreyfus RW, CN temperatures above laser ablated polyimide, Appl. Phys. A Solids Surfaces 55 (1992) 335–339, 10.1007/BF00324081.

[48]. Eckmann A, Felten A, Mishchenko A, Britnell L, Krupke R, Novoselov KS, Casiraghi C, Probing the nature of defects in graphene by Raman spectroscopy, Nano Lett. 12 (2012) 3925–3930, 10.1021/nl300901a. [PubMed: 22764888]

[49]. Gupta A, Chen G, Joshi P, Tadigadapa S, Eklund PC, Raman scattering from high-frequency phonons in supported n-graphene layer films, Nano Lett. 6 (2006) 2667–2673, 10.1021/nl061420a. [PubMed: 17163685]

[50]. Kaniyoor A, Ramaprabhu S, A Raman spectroscopic investigation of graphite oxide derived graphene, AIP Adv. 2 (2012) 1–13, 10.1063/1.4756995.

[51]. Ferrari AC, Meyer JC, Scardaci V, Casiraghi C, Lazzeri M, Mauri F, Piscanec S, Jiang D, Novoselov KS, Roth S, Geim AK, Raman spectrum of graphene and graphene layers, Phys. Rev. Lett 97 (2006) 187401, 10.1103/PhysRevLett.97.187401. [PubMed: 17155573]

[52]. Malard LM, Pimenta MA, Dresselhaus G, Dresselhaus MS, Raman spectroscopy in graphene, Phys. Rep 473 (2009) 51–87, 10.1016/j.physrep.2009.02.003.

[53]. Nam KH, Jung Kim U, Hee Jeon M, Lee TR, Yu J, You NH, Kim YK, Won Suk J, Ku BC, Green, fast, and scalable production of reduced graphene oxide via Taylor vortex flow, Chem. Eng. J 391 (2020) 123482, 10.1016/j.cej.2019.123482.

[54]. Esqueda-Barrón Y, Pérez Del Pino A, Lebière PG, Musheghyan-Avetisyan A, Bertran-Serra E, György E, Logofatu C, Boost of charge storage performance of graphene nanowall electrodes by laser-induced crystallization of metal oxide nanostructures, ACS Appl. Mater. Interfaces 13 (2021) 17957–17970, 10.1021/acsami.1c00951. [PubMed: 33843185]

[55]. Lee AY, Yang K, Anh ND, Park C, Lee SM, Lee TG, Jeong MS, Raman study of D* band in graphene oxide and its correlation with reduction, Appl. Surf. Sci 536 (2021) 147990, 10.1016/j.apsusc.2020.147990.

[56]. Vollebregt S, Ishihara R, Tichelaar FD, Hou Y, Beenakker CIM, Influence of the growth temperature on the first and second-order Raman band ratios and widths of carbon nanotubes and fibers, Carbon N. Y 50 (2012) 3542–3554, 10.1016/j.carbon.2012.03.026.

[57]. Singh SP, Li Y, Be'er A, Oren Y, Tour JM, Arnusch CJ, Laser-induced graphene layers and electrodes prevents microbial fouling and exerts antimicrobial action, ACS Appl. Mater. Interfaces 9 (2017) 18238–18247, 10.1021/acsami.7b04863. [PubMed: 28520397]

[58]. Chhetry A, Sharifuzzaman M, Yoon H, Sharma S, Xuan X, Park JY, MoS2-Decorated laser-induced graphene for a highly sensitive, hysteresis-free, and reliable piezoresistive strain sensor, ACS Appl. Mater. Interfaces 11 (2019) 22531–22542, 10.1021/acsami.9b04915. [PubMed: 31192579]

[59]. Fulvio PF, Brown SS, Adcock J, Mayes RT, Guo B, Sun XG, Mahurin SM, Veith GM, Dai S, Low-temperature fluorination of soft-templated meso-porous carbons for a high-power lithium/carbon fluoride battery, Chem. Mater 23 (2011) 4420–4427, 10.1021/cm2012395.

[60]. Nam KH, Kim K, Kim SG, Lee HS, Jung H, Yu J, Jang SG, Ku BC, Moon B, You NH, Sustainable production of reduced graphene oxide using elemental sulfur for multifunctional composites, Compos. B Eng 176 (2019) 107236, 10.1016/j.compositesb.2019.107236.

[61]. Nam K-H, Seo K, Lee S, Han H, Sulfur-doped hierarchically porous open cellular polymer/acid complex electrolyte membranes for efficient water-free proton transport, ACS Sustain. Chem. Eng 8 (2020) 16156–16163, 10.1021/acssuschemeng.0c04601.

[62]. Taylor IM, Patel NA, Freedman NC, Castagnola E, Cui XT, Direct in vivo electrochemical detection of resting dopamine using poly(3,4-ethylenedioxythiophene)/carbon nanotube functionalized microelectrodes, Anal. Chem 91 (2019) 12917–12927, 10.1021/acs.analchem.9b02904. [PubMed: 31512849]

[63]. Taylor IM, Robbins EM, Catt KA, Cody PA, Happe CL, Cui XT, Enhanced dopamine detection sensitivity by PEDOT/graphene oxide coating on in vivo carbon fiber electrodes, Biosens. Bioelectron 89 (2017) 400–410, 10.1016/j.bios.2016.05.084. [PubMed: 27268013]

[64]. Bath BD, Michael DJ, Trafton BJ, Joseph JD, Runnels PL, Wightman RM, Subsecond adsorption and desorption of dopamine at carbon-fiber microelectrodes, Anal. Chem 72 (2000) 5994–6002, 10.1021/ac000849y. [PubMed: 11140768]

[65]. Kim DH, Oh Y, Shin H, Park C, Blaha CD, Bennet KE, Kim IY, Lee KH, Jang DP, Multi-waveform fast-scan cyclic voltammetry mapping of adsorption/desorption kinetics of biogenic amines and their metabolites, Anal. Methods 10 (2018) 2834–2843, 10.1039/c8ay00352a. [PubMed: 31131044]

[66]. Venton BJ, Cao Q, Fundamentals of fast-scan cyclic voltammetry for dopamine detection, Analyst 145 (2020) 1158–1168, 10.1039/c9an01586h. [PubMed: 31922176]

[67]. Vreeland RF, Atcherley CW, Russell WS, Xie JY, Lu D, Laude ND, Porreca F, Heien ML, Biocompatible PEDOT:Nafion composite electrode coatings for selective detection of neurotransmitters in vivo, Anal. Chem 87 (2015) 2600–2607, 10.1021/ac502165f. [PubMed: 25692657]

[68]. Yang C, Jacobs CB, Nguyen MD, Ganesana M, Zestos AG, Ivanov IN, Puretzky AA, Rouleau CM, Geohegan DB, Venton BJ, Carbon nanotubes grown on metal microelectrodes for the detection of dopamine, Anal. Chem 88 (2016) 645–652, 10.1021/acs.analchem.5b01257. [PubMed: 26639609]

[69]. Yang C, Trikantzopoulos E, Jacobs CB, Venton BJ, Evaluation of carbon nanotube fiber microelectrodes for neurotransmitter detection: correlation of electrochemical performance and surface properties, Anal. Chim. Acta 965 (2017) 1–8, 10.1016/j.aca.2017.01.039. [PubMed: 28366206]

[70]. Sheng ZH, Zheng XQ, Xu JY, Bao WJ, Bin Wang F, Xia XH, Electrochemical sensor based on nitrogen doped graphene: simultaneous determination of ascorbic acid, dopamine and uric acid, Biosens. Bioelectron 34 (2012) 125–131, 10.1016/j.bios.2012.01.030. [PubMed: 22342696]

[71]. Rahman MM, Lopa NS, Ju MJ, Lee JJ, Highly sensitive and simultaneous detection of dopamine and uric acid at graphene nanoplatelet-modified fluorine-doped tin oxide electrode in the presence of ascorbic acid, J. Electroanal. Chem 792 (2017) 54–60, 10.1016/j.jelechem.2017.03.038.

[72]. Urbanová V, Karlický F, Mat j A, Šembera F, Janoušek Z, Perman JA, Ranc V, épe K, Michl J, Otyepka M, Zbo il R, Fluorinated graphenes as advanced biosensors-effect of fluorine coverage on electron transfer properties and adsorption of biomolecules, Nanoscale 8 (2016) 12134–12142, 10.1039/c6nr00353b. [PubMed: 26879645]

[73]. Nimbalkar S, Castagnola E, Balasubramani A, Scarpellini A, Samejima S, Khorasani A, Boissenin A, Thongpang S, Moritz C, Kassegne S, Ultra-capacitive carbon neural probe allows simultaneous long-term electrical stimulations and high-resolution neurotransmitter detection, Sci. Rep 8 (2018) 1–14, 10.1038/s41598-018-25198-x. [PubMed: 29311619]
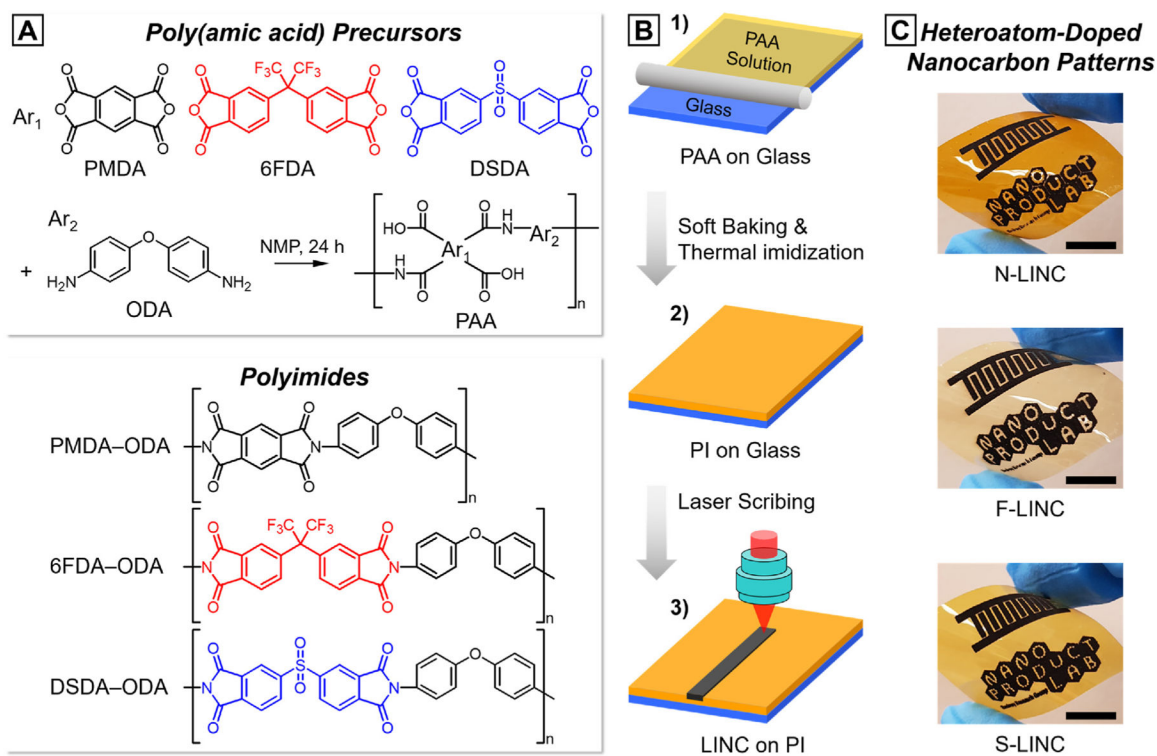
Fig. 1.

Schematic illustration of the fabrication process and demonstration of the flexible conducting platform. (a) Synthetic route and chemical structures of the three PIs. (b) Schematic procedures for the fabrication of laser-written patterns: (1) PAA precursor coated onto the glass substrate, (2) chemical transformation of PAA to PI, and (3) laser scribing to induce heteroatom-doped nanocarbon-derived pattern on the surface of the PI film. (c) Photograph of flexible laser-written patterns on different PI films (scale bar: 1 cm).
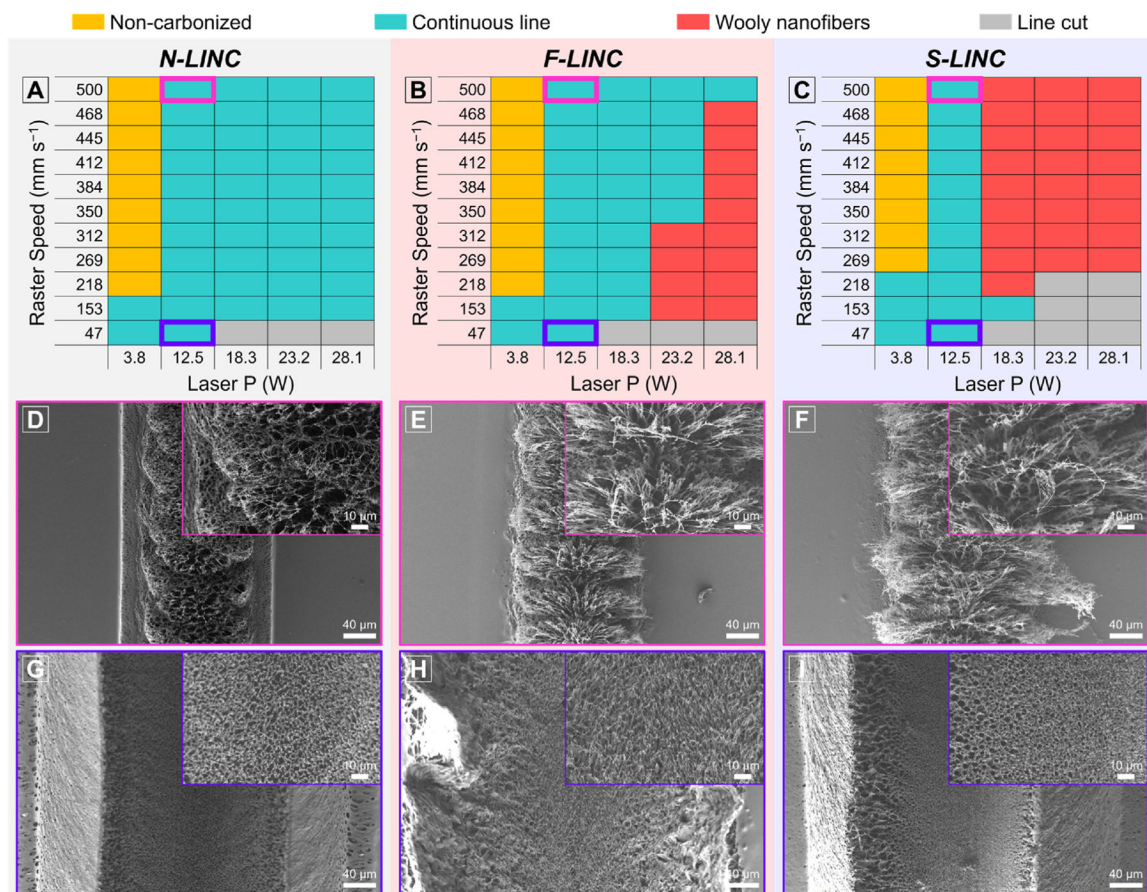
Fig. 2.
(a–c) Correlation map of laser power with raster speed on different PI backbones to achieve different doped LINC morphologies from the desired continuous lines of electrically conducting porous morphology (green) to resistive wooly nanofibers (red): (a) PMDA–ODA, (b) 6FDA–ODA, and (c) DSDA–ODA. SEM of LINC morphology for the conducting carbon lines fabricated at $P = 12.5$ W, $S = 500$ mm s^{-1} (laser fluence = 16 J cm^{-2}): (d) N-LINC, (e) F-LINC, and (f) S-LINC. SEM of LINC morphology for the conducting carbon lines fabricated at $P = 12.5$ W, $S = 47$ mm s^{-1} (laser fluence = 170 J cm^{-2}): (g) N-LINC, (h) F-LINC, and (i) S-LINC. Inset is the corresponding higher magnification SEM image.
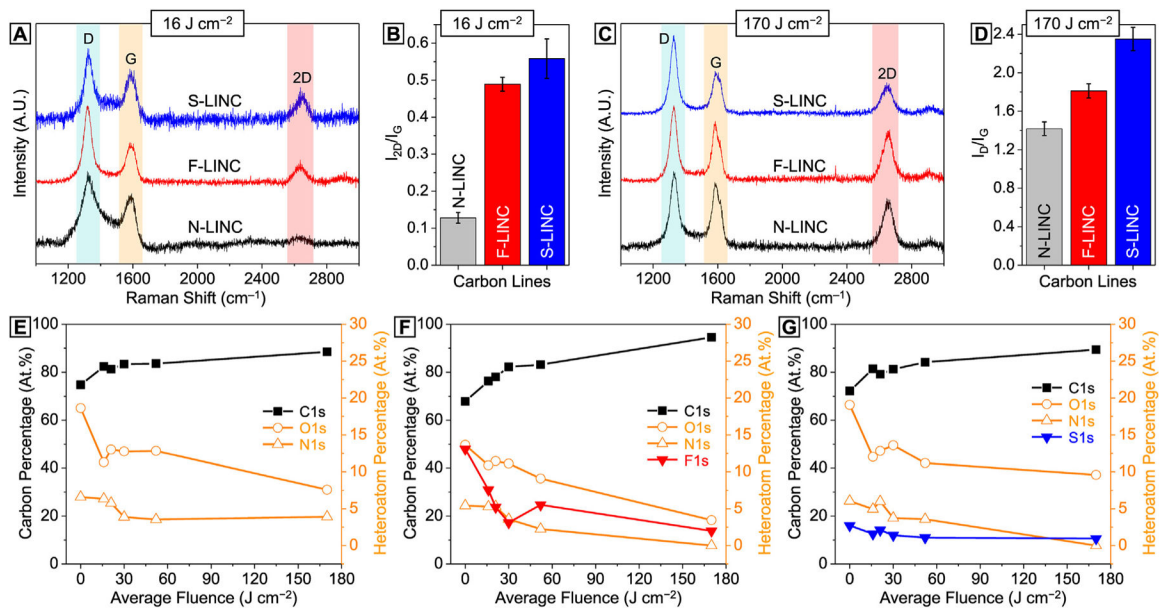
Fig. 3.

Laser fluence-dependent chemical structures of LINC. (a) Representative Raman spectra and (b) corresponding 2D/G ratio of carbon lines obtained at laser fluence of 16 J cm^{-2}. (c) Representative Raman spectra and (d) corresponding D/G ratio of carbon lines obtained at laser fluence of 170 J cm^{-2}. (e)–(g) Atomic percentages of carbon and various heteroatoms as a function of laser fluence.
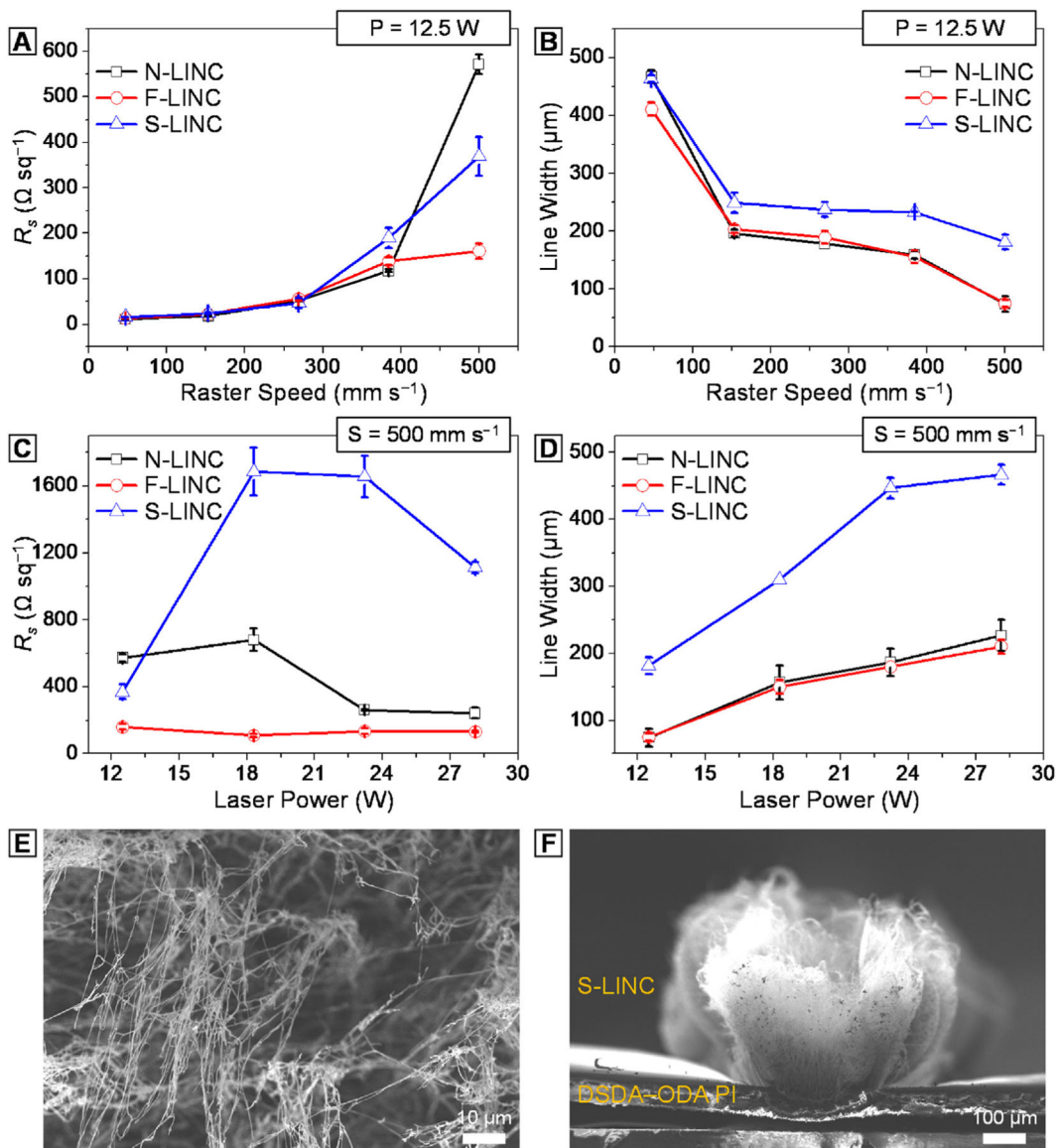
Fig. 4.
Comparison of the (a) electrode resistivity (R_s) and (b) carbonized line width of N-LINC (black line), F-LINC (red line), and S-LINC (blue line) as a function of raster speed at constant laser power of 12.5 W. Comparison of the (c) electrode resistivity (R_s) and (d) carbonized line width of N-LINC (black line), F-LINC (red line), and S-LINC (blue line) as a function of laser power at constant raster speed of 500 mm s^{-1}. (e, f) SEM of surface morphology of S-LINC fabricated at $P = 28.1$ W, $S = 500$ mm s^{-1}.
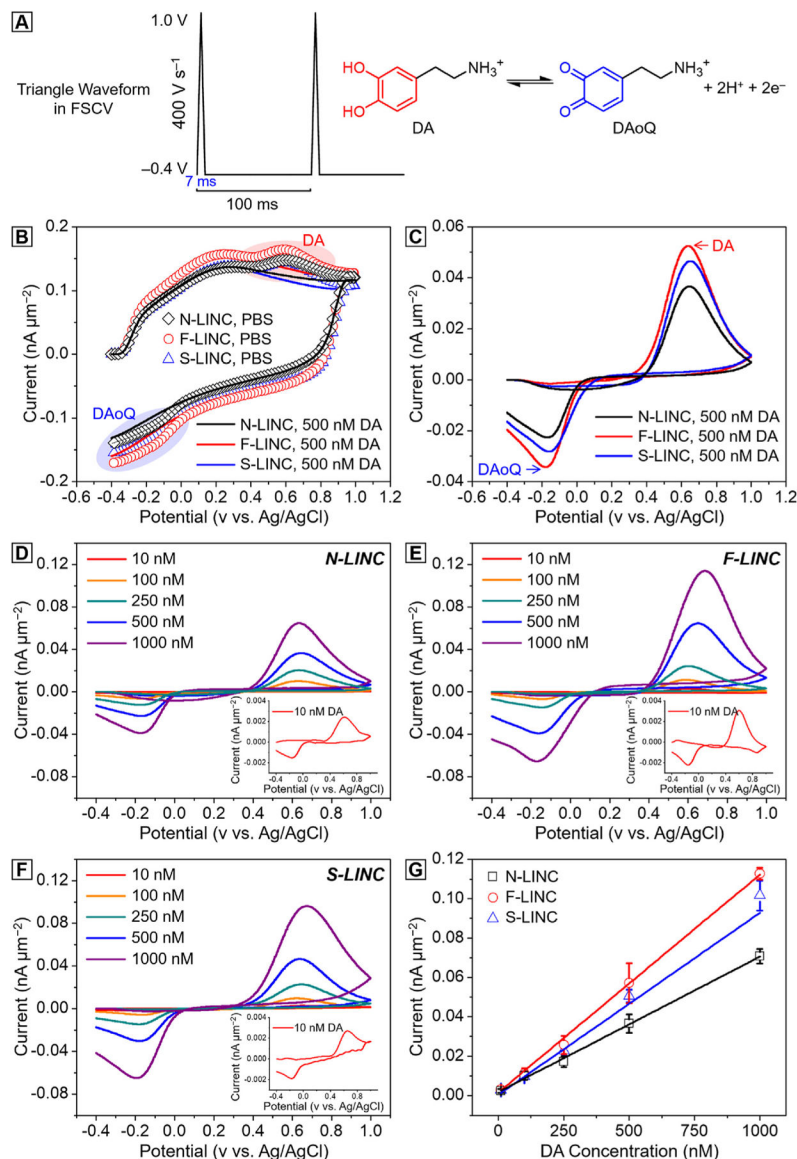
Fig. 5.
Dopamine sensitivity with three different doped LINC fabricated at P = 12.5 W, S = 47 mm s^{-1} (laser fluence = 170 J cm^{-2}). (a) Schematic of the FSCV waveform used, with holding potential −0.4 V, swhitching potential 1 V at 400 V s^{-1}, 10 Hz (left) and schematic of the two-electrons and two-protons DA reaction (right). (b) FSCV background current in PBS (lines) and in presence of 500 nM DA (scatters) for N-LINC (black), F-LINC (red), and S-LINC (blue) respectively; (c) corresponding background subtracted CVs, highlight the dopamine oxidation peaks and dopamine-o-quinone reduction peaks. Representative background subtracted CVs for 10, 100, 250, 500 nM and 1 μM bolus of DA injection collected using (d) N-LINC, (e) F-LINC, and (f) S-LINC, respectively. Inset: representative background subtracted FSCVs for 10 nM DA concentrations. (g) Calibration curves (10 nM–1.0 μM concentration range) of DA in PBS using N-LINC (black), F-LINC (red), and S-LINC (blue), respectively. Data were calibrated from 7 replicates (n = 7).